



# Spatiotemporal mapping of microscopic strains and defects to reveal Li-dendrite-induced failure in all-solid-state batteries

Hao Shen<sup>1</sup>, Kai Chen<sup>1,\*</sup>, Jiawei Kou<sup>1</sup>, Zhanhui Jia<sup>1</sup>, Nobumichi Tamura<sup>2</sup>, Weibo Hua<sup>3</sup>, Wei Tang<sup>3,\*</sup>, Helmut Ehrenberg<sup>4</sup>, Marca Doeff<sup>5,\*</sup>

<sup>1</sup> Center for Advancing Materials Performance from the Nanoscale (CAMP-Nano), State Key Laboratory for Mechanical Behavior of Materials, Xi'an Jiaotong University, Xi'an, Shaanxi 710049, China

<sup>2</sup> Advanced Light Source, Lawrence Berkeley National Laboratory, Berkeley, CA 94720, USA

<sup>3</sup> School of Chemical Engineering and Technology, Xi'an Jiaotong University, Xi'an, Shaanxi 710049, China

<sup>4</sup> Institute for Applied Materials (IAM), Karlsruhe Institute of Technology (KIT), Hermann-von-Helmholtz-Platz 1, D-76344 Eggenstein-Leopoldshafen, Germany

<sup>5</sup> Energy Storage and Distributed Resources Division, Lawrence Berkeley National Laboratory, Berkeley, CA 94720, USA

Solid-state electrolytes (SSEs) are key to the success and reliability of all-solid-state lithium batteries, potentially enabling improvements in terms of safety and energy density over state-of-the-art lithium-ion batteries. However, there are several critical challenges to their implementation, including the interfacial instability stemming from the dynamic interaction of as-formed dendritic lithium during cycling. For this work, we emphasize the importance of studying the spatial distribution and temporal evolution of strains and defects in crystalline solid-state electrolytes at the micro-scale, and how this affects dendrite growth. A proof-of-principle study is demonstrated using the synchrotron radiation based micro Laue X-ray diffraction method, and a custom-developed in-situ cycling device. Defects and residual strains are mapped, and the evolution of intragranular misorientation is observed. The feasibility of using this technique is discussed, and recommendations for micro-strain engineering to address the Li/SSEs interfacial issues are given. Also, work directions are pointed out with the consideration of combining multi-techniques for “poly-therapy”.

**Keywords:** All-solid-state Li battery; In-situ spatiotemporal  $\mu$ Laue study; Microscopic strain and defects; Dendritic failure

## Introduction

Ever growing demands for higher energy density and better safety in energy storage devices are prompting development of solid-state electrolytes (SSEs), construction of all-solid-state Li batteries (ASSLBs), and extended applications in not only electric vehicles and cell phones, but also airplanes and smart-grids [1,2]. SSEs potentially offer extraordinary advantages in reducing battery-stack volumes using a bipolar-stacked cell structure, which can potentially increase the energy densities of lithium batteries by 50% on both the device and system level [3]. The

wide operating temperature range of SSEs can also reduce the requirement for heating/cooling modules with benefits for both energy efficiency and system cost [3,4]. Since the 1960s, the scientific community has witnessed the development of diverse varieties of SSEs, many of which have excellent temperature, moisture, and electrochemical stability, high ionic conductivity, good mechanical properties, and can be processed easily [5–8].

Despite these advantages, ASSLBs still face several hurdles before they can be used in large-scale applications, such as maintaining intimate interfaces between lithium and the SSE. One of the critical challenges is the anodic failure stemming from undesirable Li dendrite or filament growth, once the cells are cycled above a critical current density [9,10]. Unfortunately, this is often too low to guarantee an acceptable performance [10,11].

\* Corresponding authors.

E-mail addresses: Chen, K. (kchenl@jmail.com), Tang, W. (tangw2018@mail.xjtu.edu.cn), Doeff, M. (mmdoeff@lbl.gov).

The growth of Li dendrites also makes fast charge and long cycle life difficult to attain. Although it is theoretically predicted that Li dendrites can be suppressed once the shear module of the SSE exceeds twice that of Li metal (4.8 GPa at room temperature) [12], Li dendrites are still observed in many SSEs with the mechanical properties satisfying the criterion. For example, Li dendrites are detected in LLZO, the shear modulus of which is over 50 GPa, more than 10 times higher than Li [13–15]. Considerable effort has been made to optimize the microstructures of the SSEs by changing the interface, density, grain size, and so on [16–20], with only limited success. There has been a long-lasting debate over the interaction mechanism between Li metal and SSEs as well as the exact origins for the formation of dendritic Li in SSEs [21–23]. Studies have been carried out to investigate this question using a variety of characterization techniques. As shown in Fig. 1, battery cycling tests have revealed the influence of interfacial resistance [11,24]. Optical and scanning electron microscopes (SEM) have been used to directly visualize the growth of dendrites, starting from flaws and then growing either along or across the grains [10,11]. Transmission electron microscopy (TEM) and computed tomography (CT) provide a direct link of microstructure to dendrite formation [25–28], while

chemical mapping studies highlight the spatial and temporal distribution of elements [26,29–31].

These efforts have shed light on the growth of Li dendrites associated with the electrochemical and mechanical synergy effects at the Li/SSEs interface, and two mechanisms have been proposed independently, which are the mechanical penetration and transport-facilitated mechanisms, respectively [32]. The former proposes that the preferred nucleation sites arise from or near the Li/SSE interface and dendrites grow directionally penetrating the SSEs. The latter emphasizes the co-relationship between the formation of lithium dendrites and the intrinsic properties of SSEs such as relatively high electronic conductivity, causing more uniform Li deposition inside the SSEs. Both mechanisms are supported by some theories and experiments but they cannot explain all phenomena observed. To date, the common mechanism for the complicated interaction between lithium anodes and SSEs remains unclear.

In the next section, we will compare the existing viewpoints on the interaction between Li and SSEs and the mechanisms in the SSE [20,23,33]. Although focusing on different aspects, researchers agree on the importance of novel and powerful materials characterization methods [23,34]. By comparing the view-

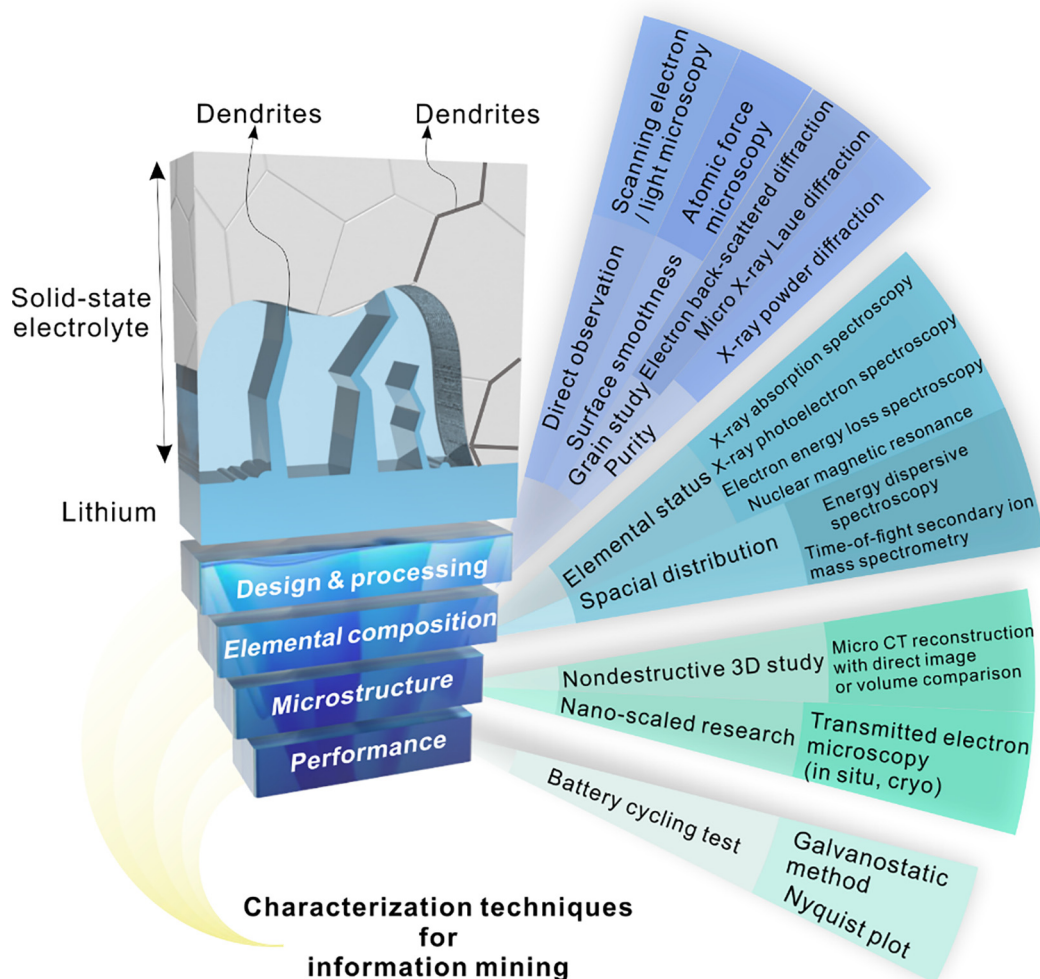


FIGURE 1

Characterization techniques applied in the main procedures from design & processing to performance testing of ASSLBs that are related to Li-induced failure.

points of these two mechanisms, we emphasize that microscopic strain, elastic and plastic, plays a key role in Li dendrite growth resulting in anodic failure as reported previously, and then highlight two key points for distinguishing the two major mechanisms of Li dendrite growth and optimization of the design of SSEs. First is mapping of the localized strains and stresses, and correlating them to the microscopic defects which originate during fabrication and processing stages, or generated during service. Second is monitoring the evolution of strains, stress, and defects under service conditions over a relatively long period of time, from the stage prior to Li dendrite nucleation until growth and short-circuit failure. Here, we apply synchrotron radiation based micro Laue X-ray diffraction ( $\mu$ Laue) to investigate strains and defects distribution in a millimeter-sized crystalline SSE, mapped with micro-scale resolution, using a custom-developed data mining method. Powered by an in-house designed in-situ cycling apparatus, the temporal evolution of defects was studied to correlate the electrochemical and mechanical behaviors under operando conditions at the early stages, even before Li dendrite nucleation. This powerful materials characterization technique can provide a more comprehensive explanation of the incipience of dendritic Li in crystalline (such as inorganic and polymer-in-ceramic composite) SSEs by electro-chemo-mechanical coupled effects, and bring insights into effective design and engineering of SSEs.

## Mechanisms of Li dendrite formation in solid-state electrolyte

### *Mechanical penetration mechanism*

The mechanical penetration mechanism emphasizes the existence of the interfacial stress due to localized high current density, and also the mechanical behavior of Li in the defects at the Li/SSE interface. Li infiltrates at pre-existing defects preferentially and eventually causes short-circuit failures. Operando optical microscopy experiments showed crack generation in polycrystalline, single-crystalline, and glassy SSEs from the contact point where the Li deposited (Fig. 2a upper) [10]. Together with atomic force microscope (AFM) results on the surface of SSEs, the relation between flaw dimension and dendrite growth was discussed. The continuous Li plating in the flaws resulted in stress build-up due to the constrained situation and opened up cracks. The stress generated is directly proportional to the overpotential, while the minimum stress needed for crack propagation is materials and geometry dependent. Thus, by considering the elastic properties of Li, an inverse square root relationship can be established to describe the Li plating overpotential and crack-propagation stress as a function of defect size [10]. Similar phenomena have also been observed using other techniques. Zhang et al. reported an operando study of Li whisker growth kinetics in an environmental TEM (ETEM) equipped with an atomic force microscope (AFM) tip, which allowed application of a potential and recording of the stress generated simultaneously (Fig. 2a bottom) [35]. Under such electro-chemo-mechanical coupled circumstances, the yield strength of micro-sized Li whiskers, which is crystal direction- and size-dependent, was up to two orders of magnitude greater of that of their polycrystalline bulky counterparts. Based on the elastic

and plastic properties of Li whiskers, a new elasto-plastic model was developed, explaining the existence of critical flaw sizes on the order of a hundred  $\mu\text{m}$ , under which no Li whisker would grow no matter how high the overpotential was [10]. In an SEM study, void formation induced SSE/anode interface failure was revealed as the cells were cycled, due to the slow replenishment rate as the Li was stripped, indicating that the elimination of pre-existing defects on the surface of SSEs was not enough to prevent formation of Li whiskers [36,37]. On the other hand, pressure-induced Coble creep of Li was shown by operando TEM experiments to be an effective approach to fill in hollow ionically and electronically conducting tubules, which allows replenishment of the stripping-induced Li loss and thus releases the stresses at the interface [38].

Thanks to the high penetration capability of high-energy X-rays and neutron beams, 3D imaging techniques such as computed tomography (CT) have been developed to visualize the structure of SSEs (even those that contain heavy elements) with decent spatial resolution [28,39–41]. Taking advantages of these features, interphase formation was evidenced directly in Li/Li<sub>10</sub>-SnP<sub>2</sub>S<sub>12</sub>/Li cells [28]. Voids formed at the interface and caused large area of contact loss between Li and SSE (Fig. 2b left). Through quantitative imaging correlation and comparison, the cell was proven to undergo a volume shrinkage due to the partial molar volume mismatch between electrodes, suggesting the importance of controlling stack stress in the all-solid-state cells [28].

Along with the mechanical penetration mechanism, some specific crack modes have been reported. For example, so-called spallation cracking was observed in a Li/Li<sub>6</sub>PS<sub>5</sub>Cl/Li symmetrical cell (Fig. 2b right), mostly in the area with high incidence of porosity, as well as the edges and corners of the electrodes where the electric field was higher due to geometrical crowding factors [27]. Combining CT and X-ray diffraction mapping, it was also shown that Li filling in the crack tips was not necessary for crack opening. Similarly, “bowl-like” cracks were discovered inside the SSE in Li/Li<sub>6.4</sub>La<sub>3</sub>Zr<sub>1.4</sub>Ta<sub>0.6</sub>O<sub>12</sub> (LLZTO) half-cells through in-situ experiments using focused ion beam (FIB)/SEM imaging, stressing that attention should be paid to not only the interface but also the bulk of SSEs [42].

In general, the mechanical penetration mechanism emphasizes the failure caused by mechanical cracking and Li deposition in the cracks. It is featured by: (1) unbalanced Li stripping and plating that result in local high current density; (2) directional crack propagation and Li infiltration starting from or near the interface; (3) continuous Li deposition as the driving force for cracks to extend; (4) significant strain/stress concentration. Based on this mechanism, to produce an SSE with improved stability under high current density, it is essential to accelerate the replenishment rate of Li, control the strain/stress at the interface, achieve high density SSEs with smooth surfaces, and optimize the mechanical properties of SSEs to resist crack growth.

### *Transport-facilitated mechanism*

In some cases, increasing the density of SSEs to modify the interfacial quality as well as strengthening their mechanical properties does not eliminate Li dendrite formation completely. Considering that Li is frequently preferentially deposited along

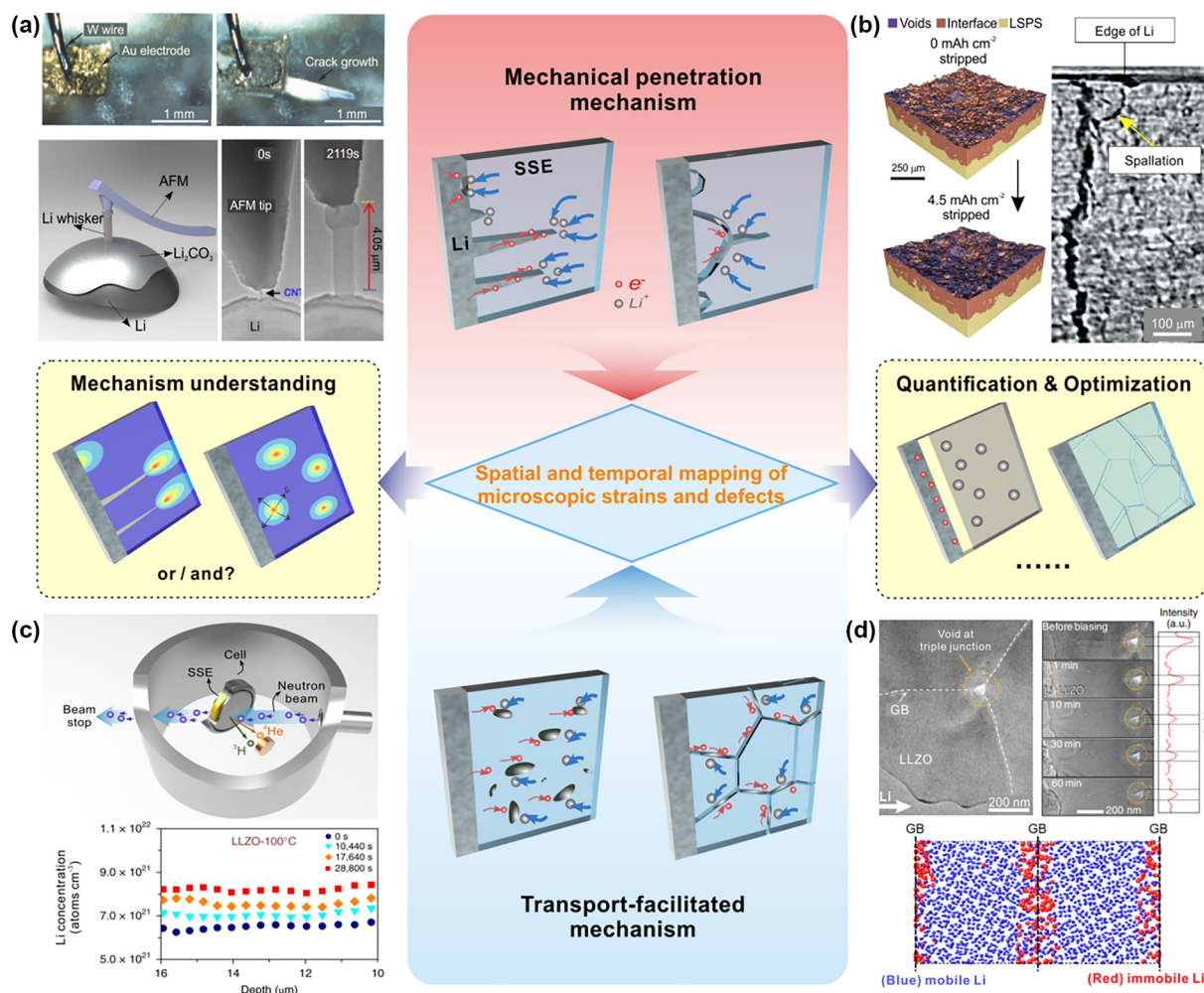


FIGURE 2

Typical experiments that support the mechanical penetration mechanism are shown in (a) and (b), and that support transport-facilitated mechanism are shown in (c) and (d). The upper image of (a) presents the operando experiment under optical microscope (reproduced from Ref. 10 with permission from Wiley-VCH). The bottom image of (a) is an operando experiment on the ETEM-AFM platform (the Li whisker figure is reproduced from Ref. 35 with permission from Nature). The bottom-left of (a) shows the setup of the platform. (b) shows the interfacial evolution (left, reproduced from Ref. 28 with permission from Nature) and spallation crack formation (right, reproduced from Ref. 27 with permission from Nature) visualized by CT. (c) is the setup and result of NDP experiment (the NDP result is reproduced from Ref. 34 with permission from Nature). The in-situ TEM (upper, reproduced from Ref. 26 with permission from Nature) and Monte Carlo (bottom, reproduced from Ref. 45 with permission from American Chemistry Society) results shows the behavior of grain boundary in (d). Through comparing the two mechanisms, spatial and temporal mapping of microscopic strains and defects are key to understanding Li-dendrite-induced failure in ASSLBs.

the grain boundaries, where the electronic conductivity may be higher than in the interior of crystal grains, a transport-facilitated mechanism is proposed. For this mechanism, the Li dendrite generation is electrochemically activated in an “overcome strength with softness” manner. The Li ions are reduced easily once meeting the free-traveling [34] or surface trapped electrons [43] and then Li dendrites nucleate at relatively arbitrary possible locations without depth preferences inside the SSEs. This mechanism also explains the proportional growth of critical current density with the operating temperature. At elevated temperatures, the Li/SSE interface quality is usually improved and thus accelerates the movement of ions and electrons to form a larger number of nucleation sites for Li dendrites. A short circuit does not occur because the surface area of Li dendrites decreases and minimizes the chances to interconnect.

The operando neutron depth profiling technique, which relies on the interaction between  $^6\text{Li}$  isotopes and neutrons, has been used to detect the Li concentration in SSEs [34]. The depth resolution of this method can be as good as tens of nanometers [44]. Interestingly, according to a comprehensive study of various SSEs including lithium phosphorus oxynitride, lithium lanthanum zirconium oxide (LLZO), and  $\text{Li}_3\text{PS}_4$ , the concentration profile of Li showed no depth-dependence (Fig. 2c), which is significantly different from the mechanical penetration mechanism. Operando TEM observations (Fig. 2d upper) and electron energy loss spectroscopy (EELS) provided direct evidence of Li deposition along grain boundaries, where the band gap decreases and electrons move more actively. Consequently, Li reduced and nucleated at the grain boundaries, grew along them, connected and finally shorted the batteries [26]. Monte Carlo simulations

with similar results suggest that low energy grain boundaries are crucial for high ion transference (Fig. 2d bottom) [45]. Phase-field simulations demonstrate that the excess trapped electrons at grain boundaries facilitate the nucleation of Li dendrites, and the dendrites grow at the highest rate when the grain boundaries are perpendicular to the Li/SSE interface [43,46].

According to the investigations, the transport-facilitated mechanism is characterized by: (1) depth/surface insensitivity and insignificant directional penetration; (2) grain boundaries as favorable nucleation sites in polycrystalline SSEs; (3) non-essential strain/stress concentration. Based on this mechanism, reducing the electronic conductivity of SSEs is the most critical way to improve performance. Some recent research on LLZO and NASICON shows that higher ionic to electronic conductivity ratios significantly improves the critical current density [47,48]. It is also mentioned that the electrical conductivity should be lower than  $10^{-10}$  S cm<sup>-1</sup> or  $10^{-12}$  S cm<sup>-1</sup> for stable cycling with current densities of 1 mA cm<sup>-2</sup> or 10 mA cm<sup>-2</sup> respectively [34].

#### *Equivocality and potential solution*

These two mechanisms highlight the different characteristics of Li dendrite growth in SSEs and point to different optimization pathways. However, they are supported by different experimental observations and theoretical predictions independently. It is even possible that the two mechanisms co-exist and contribute together to the short-circuit failure [49]. According to Li and Monroe's model based on Maxwell stress induced by space charge layers [50], the dendrite growth in LLZO is an electrochemically activated and energetically favored process. In principle, imperfect contact and concentrated defects like pores, voids and microcracks close to the interfacial region easily cause magnified local current density and thus favor Li reduction and deposition, leading to mechanical penetration. However, if the working current density is low, the mechanical toughness of the SSE is high, or the defects are distributed homogeneously in the SSE, the deposition of Li inside the SSE is expected to continue without cracking the SSE, and consequently the failure will demonstrate the characteristics of transport-facilitated mechanism. From the analysis, it is noted that the failure mode highly depends on the chemistry, microstructure (grain size and shape, grain boundary type, and so on) and working conditions of the batteries [50,51].

A comprehensive understanding of Li dendrite induced failure in ASSLBs is still unavailable for many reasons, one of which is the lack of characterization tools to monitor the driving force for Li dendrite to incubate and nucleate. At such an early stage, although it is apparent that strain/stress plays an important role, Li dendrites are too tiny to see, and thus researchers face difficulties in determining the area of interests for in-depth study. Different Li dendrite growth mechanisms are expected to result in different strain distribution characteristics. It is expected that if the transport-facilitated mechanism plays an important role, strains will increase slightly along the grain boundaries almost simultaneously from multiple positions along the thickness of the SSEs. If the mechanical penetration mechanism is predominant, localized strains will be detected preferentially near the interface, and the strains may be large enough to crack the SSEs. It is also possible that these two mechanisms co-exist, and strains

are generated at the interface and also in the bulky interior of the SSEs.

As a result, it is extremely important to develop a powerful strain/stress characterization tool with nano/micro-scale spatial resolution, millimeter-scale sampling size, decent temporal resolution, and nondestructive operando observations simultaneously. With these advantages, it becomes possible to correlate the early-stages of Li deposition, in space and time, to the strain/stress distribution and evolution, and eventually improve the electro-chemo-mechanical performance of SSEs by means of microstructure design and processing optimization. Therefore, in the following we will introduce a powerful characterization method, *i.e.* synchrotron based micro Laue X-ray diffraction ( $\mu$ Laue). Its application to the microscopic defect and micro-strain investigation of SSEs will be demonstrated and linked to the Li dendrite induced failures.

### **Microstructure and micro-strain mapping by $\mu$ Laue**

#### *Principle*

Synchrotron radiation based micro Laue X-ray diffraction is a promising tool for characterizing SSEs because of its high spatial (submicron), strain ( $10^{-4}$ ), and temporal (sub-second for each spot) resolutions. As demonstrated in Fig. 3a, since its discovery by Max von Laue and his coworkers in 1912 [52], the application of Laue diffraction was limited due to difficulties with data analysis until 1970s, when the development of synchrotron radiation brought new opportunities. In 1984, Laue diffraction data was successfully recorded and analyzed on proteins [53]. Since the 1990s, beamlines taking advantage of micro-focused polychromatic X-ray beams ( $\mu$ Laue beamlines) were established all over the world for materials microstructure study [54–61], and differential aperture methods were developed to improve the spatial resolution in the sample depth direction [62]. In the first decade of the 21st century, in-situ investigation on individual nanowires [63] and diffraction contrast tomography were realized [64]. The spatial resolution was brought down to the sub-100-nm level in 2016 [65]. With the development of hard X-ray free electron lasers, the spatial and temporal resolution of the Laue diffraction technique is expected to be further improved [66] and more dynamic study will be enabled.

In a typical  $\mu$ Laue setup, a polychromatic X-ray beam, focused to submicron size using a pair of elliptically shaped mirrors, illuminates the specimens with crystal grains larger than the X-ray beam size and generates Laue diffraction [61]. High accuracy multi-axis-motion sample stage allows the area of interest on the specimen to be scanned, and at each scanning position, with only a sub-second single exposure, a Laue pattern is recorded using a large-area 2D detector. In most cases, the experiments are carried out in reflection geometry; transmission mode is performed for thin foils only. A typical  $\mu$ Laue scan generates thousands of Laue diffraction patterns, each of which contains rich local microstructural information. Here, it has to be mentioned that the derivation of strain tensor offers a way to image the lattice distortion and strain anisotropy in the SSE. After indexing the Laue pattern, the orientation and lattice plane of each diffraction peak are known. Based on the diffraction geometry and the coordinates of diffraction peaks, it is possible to set up

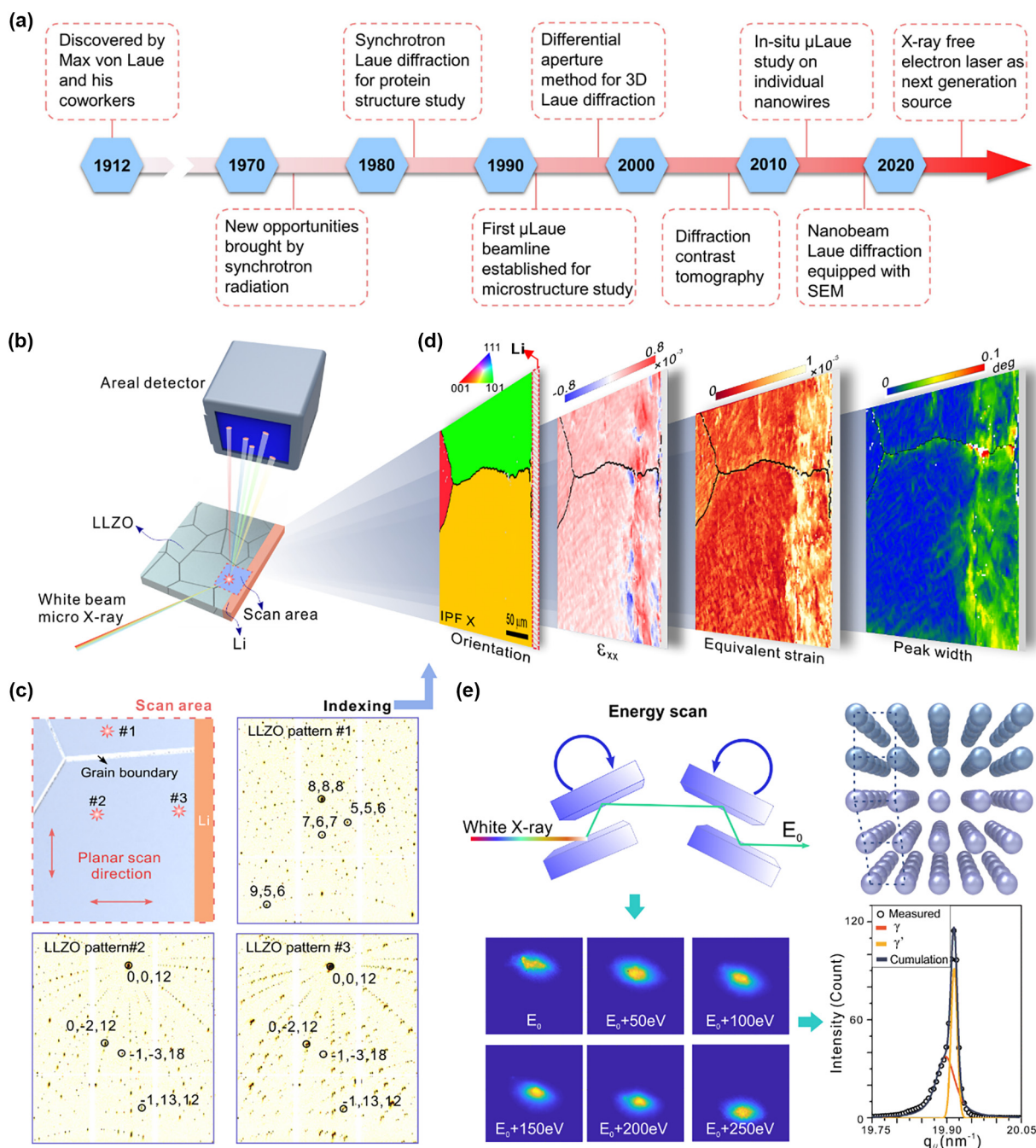


FIGURE 3

The time sequence of the development of  $\mu$ Laue is presented in (a). The setup of  $\mu$ Laue is presented in (b). (c) gives the comparison of Laue diffraction patterns in two grains (#1 and #2) and large deformation in one grain (#2 and #3). After indexing the patterns, the mappings of orientation, components of strain tensors (colorbar:  $-0.8-0.8 \times 10^{-3}$ ), von Mises equivalent strain (colorbar:  $0-1 \times 10^{-3}$ ), and peak width can be achieved in (d). The description of energy scan is shown in (e) where the upper figure shows the setup and the bottom figure shows the diffraction peak evolution with the tilt of monochromators. The mismatch of two phases is obtained in the bottom-right figure of (e).

a system of equations according to diffraction conditions and obtain the measured lattice parameters ( $a$ ,  $b$ ,  $c$ ,  $\alpha$ ,  $\beta$ , and  $\gamma$ ). Then, compared to the theoretical lattice parameters, the distortion of the lattice can be calculated using a  $3 \times 3$  tensor. Through coordinate transformation, the strain tensor can be transferred to the Cartesian coordinates established on the sample. As a result, the strain status of compression, tension, and shear along the coordinate axes can be mapped [62]. Thus, by analyzing all the Laue

patterns, the distribution of crystal structure, orientation, deviatoric elastic strain, and microscopic defects such as vacancies and dislocations in the scanned area can be mapped, and the spatial resolution is only limited by X-ray beam size and scanning step size. In addition, by inserting a monochromator in the path of the beam and tilting its incline angle in minute steps, the energy of the incident X-ray is scanned incrementally. This so-called energy scan is equivalent to the rocking curve measurement in

conventional XRD, with which local lattice constants can be measured accurately. A Si-drift detector is frequently used in a  $\mu$ Laue beamline to enable micro X-ray fluorescence chemical analysis.

From the description above, it is clear that  $\mu$ Laue differs significantly from powder diffraction. Conventional powder diffraction employs monochromatic X-ray to irradiate a great number of crystal grains to produce signals. With proper data processing, crystal structure, grain size and preferred orientations can be analyzed, but little can be known about the spatial distribution of crystal orientation, strain, and microscopic defects at the intragranular scale [67]. Such information is important to in-depth understanding of the performance of SSEs and is accessible using  $\mu$ Laue.

To demonstrate its application, the microstructure of LLZO in a symmetric Li/LLZO/Li cell was characterized using  $\mu$ Laue. The LLZO used for this test was synthesized and processed following the typical sintering procedure, and the final sample thickness was 1.11 mm and the relative density was about 90%. As displayed in Fig. 3b, the cell was mounted on the scanning stage with its cross-section facing up to the micro-focused polychromatic X-ray with an incline angle of 45°. As the synchrotron-based  $\mu$ Laue uses an X-ray white beams with continuous energy ranges from 5 keV to 24 keV, the penetration depth is about 15  $\mu$ m considering the incident angle, absorption and attenuation effect [68]. A  $260 \times 260 \mu\text{m}^2$  area covering the Li/LLZO interface was raster scanned with a scanning step size of 2  $\mu$ m (Fig. 3c). Because of the poor crystallinity and low diffraction intensity of Li, only LLZO diffraction patterns were analyzed. Clearly, the Laue patterns from different grains appear quite different, and also the diffraction peak width varied from grain boundary vicinities to the interiors. By analyzing all the 16,900 Laue patterns using the custom-developed software XMAS [69] and the peak position comparison indexing algorithm [70], crystal orientation, elastic deviatoric strain (all 6 components of the tensor as well as the von Mises equivalent strain), and diffraction peak width, which is an indicator of the microscopic defects, were successfully mapped (Fig. 3d). Three crystal grains were detected in the scanned region. The strain was lower than  $0.5 \times 10^{-3}$  on average and was high near the Li/LLZO interface. Microscopic defects were distributed in the LLZO non-homogeneously, mostly lying near the interface and along the grain boundaries. Although an energy scan was not carried out on this specimen, the diffraction peaks from two phases with a lattice mismatch of  $0.5 \times 10^{-3}$  could be unequivocally distinguished (Fig. 3e). The lattice mismatch accuracy is also dependent on crystal size, quality, and chemical composition, etc.

### Operando $\mu$ Laue study

To enable the operando  $\mu$ Laue study for the microstructure of SSEs under cycling conditions, an in-situ cycling apparatus was designed to contain two nested wide-open chambers. As shown in Fig. 4a, the same Li/LLZO/Li symmetric cell demonstrated in Fig. 3 was fixed in the inner chamber, slightly compressed mechanically with specially designed clamps to ensure electric contact between Li and SSE, and subjected to a constant current density of  $3.34 \mu\text{A}/\text{cm}^2$ . It should be noted that the applied voltage and/or current can be programmed and accurately controlled

for various purposes. Once the specimen was well aligned, the inner chamber was placed into a bigger one, which was then sealed with Kapton tape, filled with protective Ar gas, and then mounted onto the scanning stage. After the first 2 h (3 cycles) of electric current stressing, the same interfacial area was scanned, as shown in Fig. 3. Then electrical cycling tests and  $\mu$ Laue scans were repeated one more time after another 24 h cycling (16 cycles). In the last scan, the current density was doubled and continued with 3 h cycling (3 cycles), and the same area was scanned. The scans were named Scan 1 to 3 in chronological order; as a baseline, the scan prior to current stressing (displayed in Fig. 3) was named Scan 0. After indexing the obtained Laue patterns of these scans, the evolution of strain and orientation can be achieved. From the intragranular misorientation maps which are shown in Fig. 4b, it is obvious at the bottom right corner of the scan (red square) that the misorientation increased. This local misorientation increase is caused by generation of defects and large lattice distortions [71,72]. The  $\varepsilon_{zz}$  which indicates the strain along Z direction in Fig. 4c also shows similar trend.

From these results, the operando  $\mu$ Laue study proves to be relevant to the Li-dendrite-induced failure mechanism discussion. It appears that inhomogeneous residual strains were produced at the subsurface during fabrication and processing, which are more notable in larger samples. The concern about the origin of high strain at the subsurface coming from fabrication and processing is based on several reasons. Considering the  $\varepsilon_{xx}$  distribution, the plasticity of Li and hardness of LLZO, the strain should not be generated simply by compressing the symmetrical cell during mounting. According to an in-situ TEM study, the side reaction between LLZO and Li results in a phase change to the depth of only a few nanometers [25], so the strain does not result from a chemical reaction. Strain caused by sintering and polishing can be found in some reports [73,74]. On the other hand,  $\mu$ Laue is available to monitor the whole dendrite growth and development procedure through tracking strain and microstructure evolution, like what is observed in the misorientation (Fig. 4b) and  $\varepsilon_{zz}$  map (Fig. 4c). The feasibility of  $\mu$ Laue in tracking microstructure evolutions has also been proved in several works [75,76]. Detecting the incipience of Li dendrites will be highly valuable for understanding the failure behavior. To cover the whole failure procedure, more cycles, gradually increased current density (up to the order of  $1 \text{ mA}/\text{cm}^2$ ), and larger area scans that can cover both electrolyte sides are needed. Additionally, considering that thermal and mechanical impacts usually influence the formation and growth of the Li dendrites, an in-situ cycling stage with environmental and multifield coupled functions can be designed to realize low X-ray attenuation, inert gas atmosphere, mechanical stress application and feedback, and accurate temperature control (Fig. 4d).

Energy scans will be also helpful to answer directly whether lattice volume changes will occur due to ion transference and space charging, especially near the interface and grain boundaries. Many other open questions require more systematic study, for example, how testing temperature and interface modification influence strain distribution, how grain size and grain boundary types impact failure mode, and so on. The study of microstructure and strains with spatial and temporal resolution

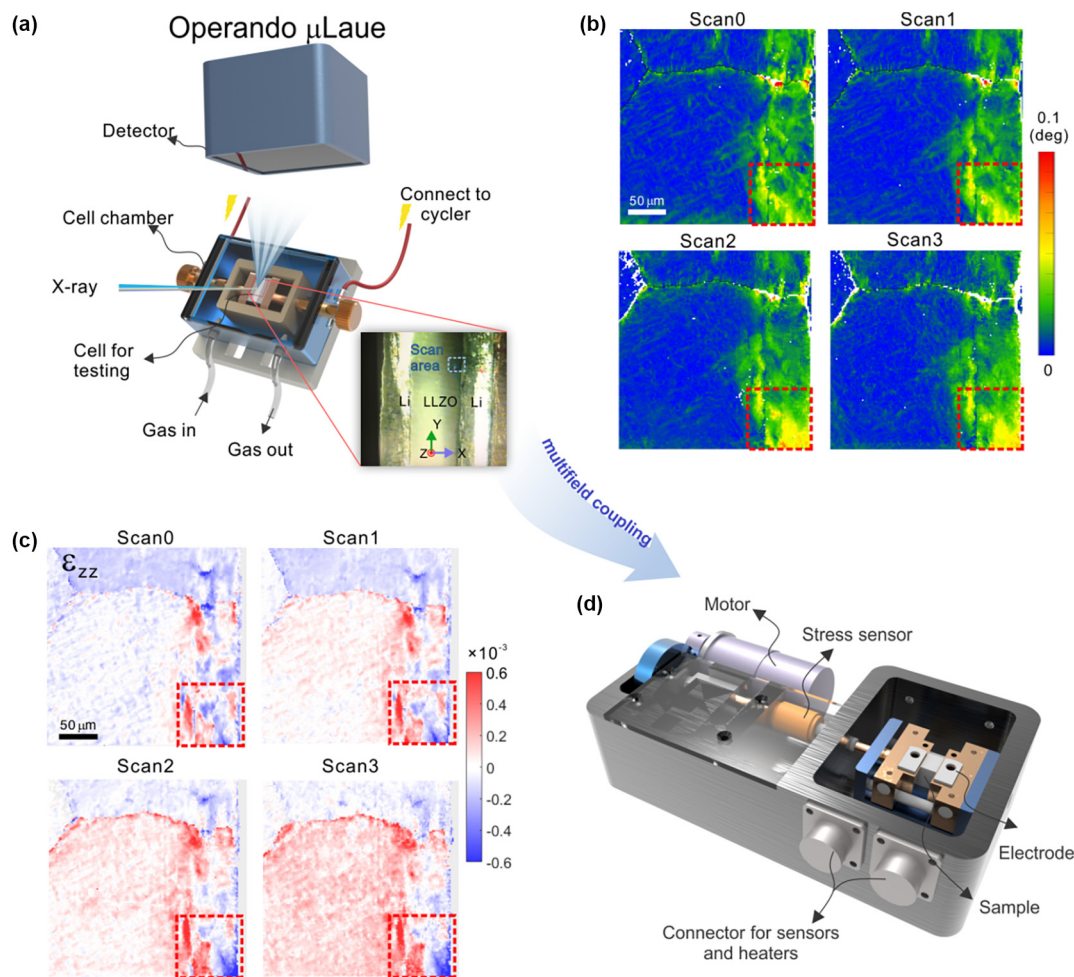


FIGURE 4

The setup of operando  $\mu$ Laue is given in (a). The insert is the optical photo of the detected Li/LLZO/Li cell. (b) is the evolution of intragranular misorientation of the whole detected area. The area in the red rectangle shows obvious increases in misorientation. (c) is the strain evolution along Z direction. (d) is the in-situ stage which can apply multifield study on ASSLB.

helps establish the relationship between fabrication parameters and electro-mechano-chemistry of SSEs, which can ultimately lead to improved performance of all-solid-state batteries.

#### Qualification of strain and ionic conductivity in SSEs

Strains can be introduced into SSEs during manufacturing, especially from the sintering [73,77] and stacking [78] procedures, and can also accumulate during cycling either because of mass diffusion or volume changes stemming from the cathode [79]. The strains are distributed inhomogeneously and inconstantly as a function of position and time, thus strain mapping is important not only for revealing the failure mechanism, but also for optimizing the ionic conductivity via elastic strain engineering, because it has been proved that the distortion and dilatation of SSE lattices leads to variation in ionic migration barriers. Considering effects of the hydrostatic stress, or pressure, only, the ionic conductivity is expressed by the following equation:

$$\frac{\partial \ln(\sigma)}{\partial P} = \frac{\beta}{3} - \frac{V_a}{k_B T}$$

where  $\sigma$  is the ionic conductivity,  $P$  the pressure,  $\beta$  the material compressibility,  $V_a$  the activation volume,  $k_B$  the Boltzmann constant, and  $T$  the temperature.

The activation volume  $V_a$ , which could be either negative or positive [80], is materials dependent. Compressive strain/stress promotes the ionic conductivity for materials with negative activation volume, such as Li- $\beta$ - $\text{Al}_2\text{O}_3$ , but for K- $\beta$ - $\text{Al}_2\text{O}_3$  the activation volume of which is positive, tensile stress/strain favors ionic conduction. Ion migration energy barriers increase when the applied strain results in a bottleneck for ion migration in lithium lanthanum titanate (LLT) with the perovskite structure, and lithium germanium phosphosulfide (LGPS) [81,82]. The mechanical pressure theoretically will impede ion transference in  $\text{Na}_3\text{PS}_4$  due to the lattice volume decrease, but better densification and mobile sodium defects can offset the negative influence [83]. Based on the recent simulations, the highest Li self-diffusivity is obtained in LLZO strained by 2 GPa tensile stress [83]. Considering the existence of a large population of oxygen vacancies in LLZO, the induced strains are expected to influence Li ion transfer and phase stability.

Therefore, strain mapping benefits the processing of SSEs and the design of all solid-state batteries, especially for thick composite electrodes.

## Summary and outlook

### The evolved $\mu$ Laue techniques

In this article, we have summarized the two commonly proposed mechanisms for Li dendrite-induced short-circuit failure and relevant characteristic results, and introduced the high-resolution microscopic strain and defect mapping technique as an important tool to better understand the incipience of Li dendrite formation in SSEs. A proof of principle experiment has proven the feasibility of  $\mu$ Laue in operando SSE cycling studies, which offers the feasibility to understand, mitigate, and even prevent the Li dendrite-induced short circuit failure in the ASSLBs.

It is obvious that ASSLBs are under electro-chemo-mechanical coupling conditions. As a result, it is necessary to develop a comprehensive characterization approach for visualizing the distribution and evolution of morphology, strain/stress, chemical concentration, and valence state [84]. In line with this,  $\mu$ Laue can be combined with other synchrotron radiation based techniques such as micro/nano-CT, and X-ray absorption spectroscopy [85] (Fig. 5a) to collect the mechanical, chemical, electrical, and morphological information at multi-scale and -dimensions simultaneously.

The recently developed technique, diffraction contrast tomography, combines the functions of both CT and  $\mu$ Laue to some extent [86,87] and has demonstrated the power to characterize the grain morphology, orientation, and strain/stress distribution in three dimensions. Diffraction contrast tomography has been successfully applied to study the grain boundary migration during grain growth in polycrystals (Fig. 5b) [88], identify the 3D phase, grain and strain distribution in polycrystalline photovoltaic materials, and map the symmetry-breaking strain fields in ferroelectric ceramic materials [89]. This method promises to shed light on understanding the interaction between Li metal and SSEs.

### Poly-therapeutic studies using synchrotron techniques

In addition to the combination of CT and  $\mu$ Laue, the synchrotron radiation based hard XRD-CT, which is a combination of X-ray powder diffraction and CT using a micro-sized X-ray beam, has also been reported recently for operando battery studies with high spatial resolution of approximately  $1\ \mu\text{m}$  [90,91]. Although a large quantity of data is produced by the scans of both transverse and angular directions, a Parameter Quantification Network based data analysis approach has been developed to realize the real time nondestructive microstructural visualization [92]. After Rietveld refinement of the powder diffraction 1D curves and rendering tomographic reconstruction using the

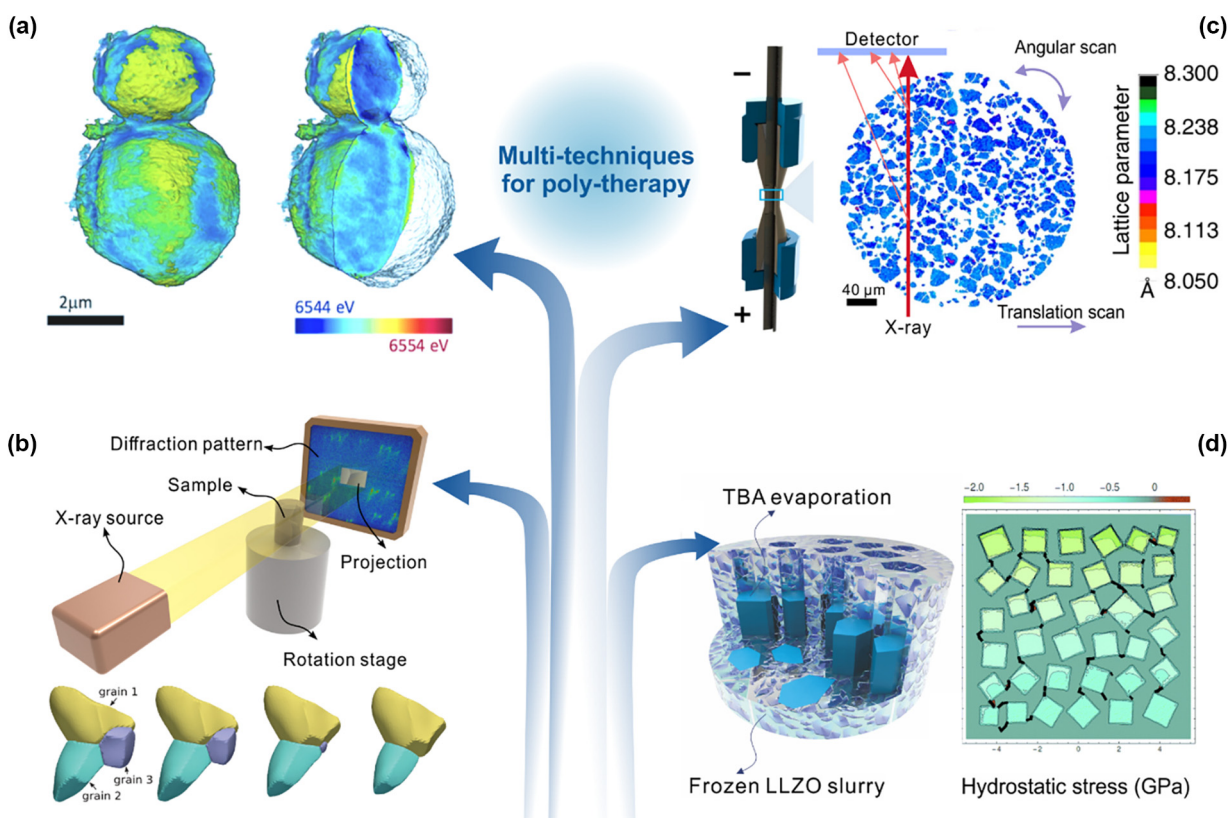


**FIGURE 5**

Combination of multi characterization techniques can benefit further study, including (a) the combination of elemental mapping and tomography (reproduced from Ref. 85 with permission from Elsevier), (b) DCT (the bottom figure is reproduced from Ref. 88 with permission from Elsevier), and (c) hard XRD-CT experiment (reproduced from Ref. 90 with permission from Nature). For the composite electrode with SSE framework as (d), the strain mapping is also essential (left figure is reproduced from Ref. 106 with permission from Royal Society of Chemistry, right figure is reproduced from Ref. 79 with permission from Royal Society of Chemistry).

selected Bragg reflections, the internal phase changes are identified and the stoichiometric variations are mapped in the bulk battery during cycling. In order to increase the spatial and temporal resolution, the data collection strategy has been improved [93], and the inter- and intra-granular response of distinct sub-micron-sized  $\text{Li}_x\text{Mn}_2\text{O}_4$  electrode particles were successfully characterized [90]. In spite of such great application potentials, however, XRD-CT is not an ideal option to study the microstructures for crystal grains coarser than the micro-focused X-ray beam size, because powder diffraction cannot be fully carried out. Unfortunately, many SSEs fall into this unavailable range, such as LLZO. Consequently, the idea of combining XRD-CT with  $\mu\text{Laue}$  probably brings new opportunities to electrodes composed of inhomogeneous particles, such as a system of coarse-grained LLZO and nano/submicron-sized NMC. With optimized experimental procedures, it is possible that the Laue and powder diffraction signals from LLZO and NMC, respectively, can be collected in a single scan, and thus the 3D microstructure spatial distribution and its temporal evolution during cycling can be understood comprehensively.

The applicable synchrotron based in-situ techniques potentially helpful to the ASSLB community are listed in Table 1. The temporal resolution of these techniques is highly dependent of the incident X-ray quality, sample status, and experimental setup.

So far there are limited reports on the combination of spectroscopic and diffraction methods, and the difficulties lie in the fact that different types of detectors and sample environments are required for these techniques and the wavelength and collimation of the incident X-ray beams are different. It is equally important to cross check the synchrotron results with TEM, which provides unprecedented spatial resolution down to the sub-atomic scale. The combination of these techniques not only

provides comprehensive information on the electrochemical and structural characteristics of the batteries, but also covers a larger portion of the specimens, avoiding the disadvantages of either poor spatial resolution or lack of representativeness suffered by the individual characterization techniques.

#### Outlook: potential directions for materials design

With various characterization techniques applied to all-solid-state battery studies, microscopic strain and defects can be mapped with high spatial and temporal resolutions, and their evolution may be directly correlated to the electro-chemo-mechanical conditions and processes. These multi-dimensional trans-scale poly-therapeutic studies will provide important information to answer unequivocally: (1) what the dominant driving force is for the Li dendrites to nucleate and grow; (2) what the preferential pathways are for the Li dendrites to propagate and/or to connect with one another.

Furthermore, local microstructure characteristics of the SSEs deserve more attention. Conventionally, either stack pressure [36] or intrinsic mechanical properties, such as Young's modulus, hardness and fracture toughness, is measured as bulk values [32]. However, inhomogeneity is inevitable in the SSEs. For example, residual strains are concentrated along the grain boundaries although the overall pressure is low in a spark plasma sintered SSE [98]. Consequently, high spatial and temporal resolution measurements of strain and defects under operando electrochemical conditions offer indicators to evaluate and optimize the design and construction of SSEs. The indicators include but are not limited to the spatial distributions and temporal evolutions of residual strains, grain size and shape, preferred crystallographic orientation, intra-granular misorientation, grain boundary geometry and misorientation, lattice mismatch at the interface, pore geometry and so on. Grain boundary

TABLE 1

Summary of synchrotron based characteristic methods potentially useful for ASSLB study.

Synchrotron radiation based characteristic techniques	Features	Sample geometry	Spatial resolution	Temporal resolution	Dimension of imaging	References
$\mu\text{Laue}$	Microstructure study including strain tensor, orientation, dislocations, and etc.	Bulk, size limit depends on the moving distance of sample stage	$\sim 100$ nm – several micrometers	Hundreds of milliseconds per pattern	2D/3D (with wire scan)	[84]
Micro/Nano CT	Morphological study including interface, pores, cracks and etc.	Bulk, dimension depends on penetration depth	$\sim 10$ nm – several micrometers (voxel)	Minutes – hours	3D	[94]
Diffraction contrast tomography (DCT)	Morphological study of coarse grains or single crystal with strain and orientation distribution information	Bulk, grain size larger than beam size	Sub-micron – several micrometers (voxel)	Tens of minutes – hours	3D	[88]
XRD-CT	Morphological study of small grains with phase distribution	Bulk, grain size much smaller than beam size	Several micrometers (voxel)	<2 mins – hours	3D	[90,95]
X-ray absorption spectroscopy: X-ray absorption near edge structure (XANES) and extended X-ray absorption fine structure (EXAFS)	Elemental analysis with chemical and structural information included	Particles, thin pieces	Tens of nanometers – several micrometers	Seconds – hours	1D/2D	[96]
TXM-XANES	Morphological and chemical structural information	Single particle	Tens of nanometers	Several minutes – tens of minutes	2D/3D	[97]

modification and polymer in ceramic “hybrid” SSEs can also be investigated by the means introduced in this review [99–101].

More sophisticated battery designs are proposed recently, e.g., using 3D composite electrode and/or electrolyte frames [8,102–108] to improve energy density, relieving stresses from Li metal by Coble creep [38], and using multilayer composite solid electrolytes [109,110]. When innovative 3D structures are applied in all-solid-state batteries (Fig. 5d), more detailed studies need to be executed, for instance the strain distribution in multiple dimensions, lattice mismatch control at the interface, and geometric structure control. The effective research tools and innovative battery design can finally pave the way to all-solid-state batteries with high stability and long cycling life.

### Declaration of Competing Interest

The authors declare that they have no known competing financial interests or personal relationships that could have appeared to influence the work reported in this paper.

### Acknowledgements

This work was supported by the National Key R&D Program of China (2021YFB2400400), National Science and Technology Major Project (2019-VII-0019-0161), the Assistant Secretary for Energy, Efficiency and Renewable Energy, Office of Vehicle Technologies of the U.S. Department of Energy under Contract No. DE-AC02-05CH11231, National Natural Science Foundation of China (Grant Nos. 51927801, 21905220, 22108218, U20322205), and 111 Project 2.0 (BP0618008). The ALS is supported by the Director, Office of Science, Office of Basic Energy Sciences, Materials Science Division, of the U.S. Department of Energy under Contract No. DE-AC02-05CH11231 at LBNL.

This document was prepared as an account of work sponsored by the United States Government. While this document is believed to contain correct information, neither the United States Government nor any agency thereof, nor the Regents of the University of California, nor any of their employees, makes any warranty, express or implied, or assumes any legal responsibility for the accuracy, completeness, or usefulness of any information, apparatus, product, or process disclosed, or represents that its use would not infringe privately owned rights. Reference herein to any specific commercial product, process, or service by its trade name, trademark, manufacturer, or otherwise, does not necessarily constitute or imply its endorsement, recommendation, or favoring by the United States Government or any agency thereof, or the Regents of the University of California. The views and opinions of authors expressed herein do not necessarily state or reflect those of the United States Government or any agency thereof or the Regents of the University of California.

### References

- [1] S. Xia et al., *Chem* 5 (4) (2019) 753–785, <https://doi.org/10.1016/j.chempr.2018.11.013>.
- [2] X. Gao et al., *Joule* 4 (9) (2020) 1864–1879, <https://doi.org/10.1016/j.joule.2020.06.016>.
- [3] T. Famprikis et al., *Nat. Mater.* 18 (12) (2019) 1278–1291, <https://doi.org/10.1038/s41563-019-0431-3>.
- [4] P. Bai et al., *Energy Environ. Sci.* 9 (10) (2016) 3221–3229, <https://doi.org/10.1039/c6ee01674j>.
- [5] Z. Zhang et al., *Energy Environ. Sci.* 11 (8) (2018) 1945–1971, <https://doi.org/10.1039/c8ee01053f>.
- [6] S. Afyon, F. Krumeich, J.L.M. Rupp, *J. Mater. Chem. A* 3 (36) (2015) 18636–18648, <https://doi.org/10.1039/c5ta03239c>.
- [7] F. Han et al., *Adv. Energy Mater.* 6 (8) (2016) 1501590, <https://doi.org/10.1002/aenm.201501590>.
- [8] H. Shen et al., *Sustain. Energy Fuels* 3 (7) (2019) 1647–1659, <https://doi.org/10.1039/c9se00119k>.
- [9] E.J. Cheng, A. Sharafi, J. Sakamoto, *Electrochim. Acta* 223 (2017) 85–91, <https://doi.org/10.1016/j.electacta.2016.12.018>.
- [10] L. Porz et al., *Adv. Energy Mater.* 7 (20) (2017) 1701003, <https://doi.org/10.1002/aenm.201701003>.
- [11] A. Sharafi et al., *J. Power Sources* 302 (2016) 135–139, <https://doi.org/10.1016/j.jpowsour.2015.10.053>.
- [12] C. Monroe, J. Newman, *J. Electrochem. Soc.* 152 (2) (2005) A396–A404, <https://doi.org/10.1149/1.1850854>.
- [13] J.E. Ni et al., *J. Mater. Sci.* 47 (23) (2012) 7978–7985, <https://doi.org/10.1007/s10853-012-6687-5>.
- [14] Y. Ren et al., *Electrochem. Commun.* 57 (2015) 27–30, <https://doi.org/10.1016/j.elecom.2015.05.001>.
- [15] A.-N. Wang et al., *J. Eur. Ceram. Soc.* 38 (9) (2018) 3201–3209, <https://doi.org/10.1016/j.jeurceramsoc.2018.02.032>.
- [16] X. Han et al., *Nat. Mater.* 16 (5) (2017) 572–579, <https://doi.org/10.1038/nmat4821>.
- [17] L. Cheng et al., *Phys. Chem. Chem. Phys.* 16 (34) (2014) 18294–18300, <https://doi.org/10.1039/c4cp02921f>.
- [18] H. Duan et al., *J. Am. Chem. Soc.* 140 (1) (2018) 82–85, <https://doi.org/10.1021/jacs.7b10864>.
- [19] C. Wang et al., *Adv. Energy Mater.* 8 (6) (2017) 1701963, <https://doi.org/10.1002/aenm.201701963>.
- [20] C. Wang et al., *Chem. Rev.* 120 (2020) 4257–4300, <https://doi.org/10.1021/acs.chemrev.9b00427>.
- [21] J. Liu et al., *Adv. Energy Mater.* 12 (4) (2021) 2100748, <https://doi.org/10.1002/aenm.202100748>.
- [22] Y. Song et al., *Adv. Energy Mater.* 9 (21) (2019) 1900671, <https://doi.org/10.1002/aenm.201900671>.
- [23] Y. Tang et al., *Energy Environ. Sci.* 14 (2) (2021) 602–642, <https://doi.org/10.1039/d0ee02525a>.
- [24] J. Glöckner et al., *J. Power Sources* 359 (2017) 157–165, <https://doi.org/10.1016/j.jpowsour.2017.05.037>.
- [25] C. Ma et al., *Nano Lett.* 16 (11) (2016) 7030–7036, <https://doi.org/10.1021/acs.nanolett.6b03223>.
- [26] X. Liu et al., *Nat. Mater.* 20 (11) (2021) 1485–1490, <https://doi.org/10.1038/s41563-021-01019-x>.
- [27] Z. Ning et al., *Nat. Mater.* 20 (2021) 1121–1129, <https://doi.org/10.1038/s41563-021-00967-8>.
- [28] J.A. Lewis et al., *Nat. Mater.* 20 (2021) 503–510, <https://doi.org/10.1038/s41563-020-00903-2>.
- [29] K. Park et al., *Chem. Mater.* 28 (21) (2016) 8051–8059, <https://doi.org/10.1021/acs.chemmater.6b03870>.
- [30] M. Kubicek et al., *Chem. Mater.* 29 (17) (2017) 7189–7196, <https://doi.org/10.1021/acs.chemmater.7b01281>.
- [31] L. Cheng et al., *J. Mater. Chem. A* 2 (1) (2014) 172–181, <https://doi.org/10.1039/c3ta13999a>.
- [32] T. Krauskopf et al., *Chem. Rev.* 120 (15) (2020) 7745–7794, <https://doi.org/10.1021/acs.chemrev.0c00431>.
- [33] K.B. Hatzell et al., *ACS Energy Lett.* 5 (3) (2020) 922–934, <https://doi.org/10.1021/acseenergylett.9b02668>.
- [34] F. Han et al., *Nat. Energy* 4 (3) (2019) 187–196, <https://doi.org/10.1038/s41560-018-0312-z>.
- [35] L. Zhang et al., *Nat. Nanotechnol.* 15 (2) (2020) 94–98, <https://doi.org/10.1038/s41565-019-0604-x>.
- [36] J. Kasemchainan et al., *Nat. Mater.* 18 (10) (2019) 1105–1111, <https://doi.org/10.1038/s41563-019-0438-9>.
- [37] T. Krauskopf et al., *ACS Appl. Mater. Interfaces* 11 (2019) 14463–14477, <https://doi.org/10.1021/acsaami.9b02537>.
- [38] Y. Chen et al., *Nature* 578 (7794) (2020) 251–255, <https://doi.org/10.1038/s41586-020-1972-y>.
- [39] W.-A. Kahl, C. Hansen, W. Bach, *Solid Earth* 7 (2) (2016) 651–658, <https://doi.org/10.5194/se-7-651-2016>.
- [40] B. Song et al., *Chem. Mater.* 31 (1) (2018) 124–134, <https://doi.org/10.1021/acs.chemmater.8b03199>.
- [41] B. Song et al., *ACS Energy Lett.* 4 (10) (2019) 2402–2408, <https://doi.org/10.1021/acseenergylett.9b01652>.

- [42] J. Zhao et al., *Energy Environ. Mater.* (2022), <https://doi.org/10.1002/eeem.12261>.
- [43] H.-K. Tian et al., *Chem. Mater.* 31 (18) (2019) 7351–7359, <https://doi.org/10.1021/acs.chemmater.9b01967>.
- [44] R.G. Downing et al., *J. Res. Natl. Inst. Stand. Technol.* 98 (1) (1993) 109–126, <https://doi.org/10.6028/jres.098.008>.
- [45] S. Yu, D.J. Siegel, *Chem. Mater.* 29 (22) (2017) 9639–9647, <https://doi.org/10.1021/acs.chemmater.7b02805>.
- [46] K. Tantratian et al., *Adv. Energy Mater.* 11 (13) (2021) 2003417, <https://doi.org/10.1002/aenm.202003417>.
- [47] W. Ping et al., *Adv. Energy Mater.* 10 (25) (2020) 2000702, <https://doi.org/10.1002/aenm.202000702>.
- [48] X. Wang et al., *Chem. Eng. J.* 427 (2022), <https://doi.org/10.1016/j.cej.2021.130899> 130899.
- [49] E. Kazyak et al., *Matter* 2 (4) (2020) 1025–1048, <https://doi.org/10.1016/j.matt.2020.02.008>.
- [50] G. Li, C.W. Monroe, *Phys. Chem. Chem. Phys.* 21 (36) (2019) 20354–20359, <https://doi.org/10.1039/c9cp03884a>.
- [51] A. Sharafi et al., *J. Mater. Chem. A* 5 (40) (2017) 21491–21504, <https://doi.org/10.1039/c7ta06790a>.
- [52] J.L. Amorós, M.J. Buerger, *The Laue method*, Academic Press, New York, 1975.
- [53] K. Moffat, D. Szebenyi, D. Bilderback, *Science* 223 (4643) (1984) 1423–1425, <https://doi.org/10.1126/science.223.4643.1423>.
- [54] G.E. Ice, *Xray Spectrom.* 26 (6) (1997) 315–326, [https://doi.org/10.1002/\(SICI\)1097-4539\(199711/12\)26:6<315::AID-XRS229>3.0.CO;2-N](https://doi.org/10.1002/(SICI)1097-4539(199711/12)26:6<315::AID-XRS229>3.0.CO;2-N).
- [55] J.-S. Chung, G.E. Ice, *J. Appl. Phys.* 86 (1999) 5249–5255, <https://doi.org/10.1063/1.371507>.
- [56] N. Tamura et al., *J. Synchrotron Rad.* 10 (2) (2003) 137–143, <https://doi.org/10.1107/s0909049502021362>.
- [57] F. Hofmann et al., *Procedia Eng.* 1 (2009) 193–196, <https://doi.org/10.1016/j.proeng.2009.06.045>.
- [58] J.G. Hamilton et al., *ACS Earth Space Chem.* 2 (11) (2018) 1161–1167, <https://doi.org/10.1021/acsearthspacechem.8b00063>.
- [59] O. Ulrich et al., *Rev. Sci. Instrum.* 82 (3) (2011), <https://doi.org/10.1063/1.3555068>. PMID: 21456764 033908.
- [60] O. Robach et al., *Laue microdiffraction at the ESRF*, in: R. Barabash, G. Ice (Eds.), *Strain and Dislocation Gradients from Diffraction: Spatially Resolved Local Structure and Defects*, Imperial College Press, London, 2014, pp. 156–204, [https://doi.org/10.1142/9781908979636\\_0005](https://doi.org/10.1142/9781908979636_0005).
- [61] M. Kunz et al., *Rev. Sci. Instrum.* 80 (3) (2009), <https://doi.org/10.1063/1.3096295> 035108.
- [62] B.C. Larson et al., *Nature* 415 (6874) (2002) 887–890, <https://doi.org/10.1038/415887a>.
- [63] H. Guo et al., *Nano Lett.* 11 (8) (2011) 3207–3213, <https://doi.org/10.1021/nl201460v>.
- [64] W. Ludwig et al., *J. Appl. Cryst.* 41 (2008) 302–309, <https://doi.org/10.1107/S0021889808001684>.
- [65] X. Chen et al., *MRS Bull.* 41 (2016) 445–453, <https://doi.org/10.1557/mrs.2016.97>.
- [66] K. Moffat, *Phil. Trans. R. Soc. A* 377 (2019) 20180243, <https://doi.org/10.1098/rsta.2018.0243>.
- [67] P. Barai et al., *Chem. Mater.* 33 (12) (2021) 4337–4352, <https://doi.org/10.1021/acs.chemmater.0c04393>.
- [68] L. Cheng et al., *ACS Appl. Mater. Interfaces* 7 (3) (2015) 2073–2081, <https://doi.org/10.1021/am508111r>.
- [69] N. Tamura, XMAS: A versatile tool for analyzing synchrotron X-ray microdiffraction data, in: R. Barabash, G. Ice (Eds.), *Strain and Dislocation Gradients from Diffraction: Spatially Resolved Local Structure and Defects*, Imperial College Press, London, 2014, pp. 125–155, [https://doi.org/10.1142/9781908979636\\_0004](https://doi.org/10.1142/9781908979636_0004).
- [70] J. Kou, K. Chen, N. Tamura, *Scr. Mater.* 143 (2018) 49–53, <https://doi.org/10.1016/j.scriptamat.2017.09.005>.
- [71] M.P. Popovic et al., *Acta Mater.* 151 (2018) 301–309, <https://doi.org/10.1016/j.actamat.2018.03.041>.
- [72] M.G. Tsoutsouva et al., *Acta Mater.* 8 (2015) 112–120, <https://doi.org/10.1016/j.actamat.2015.01.012>.
- [73] V.R. Vedula et al., *J. Am. Ceram. Soc.* 84 (12) (2001) 2947–2954, <https://doi.org/10.1111/j.1151-2916.2001.tb01119.x>.
- [74] T. Suratwala et al., *J. Non. Cryst. Solids* 352 (52–54) (2006) 5601–5617, <https://doi.org/10.1016/j.jnocrsol.2006.09.012>.
- [75] H. Shen et al., *Sci. Rep.* 6 (2016) 24418, <https://doi.org/10.1038/srep24418>.
- [76] K. Chen et al., *Adv. Mater.* 32 (2020) 1907164, <https://doi.org/10.1002/adma.201907164>.
- [77] H. Yamada et al., *J. Power Sources* 368 (2017) 97–106, <https://doi.org/10.1016/j.jpowsour.2017.09.076>.
- [78] Z.-H. Fu et al., *Energy Fuels* 35 (12) (2021) 10210–10218, <https://doi.org/10.1021/acs.energyfuels.1c00488>.
- [79] G. Bucci et al., *J. Mater. Chem. A* 5 (36) (2017) 19422–19430, <https://doi.org/10.1039/c7ta03199h>.
- [80] T. Famprikis et al., *J. Am. Chem. Soc.* 142 (43) (2020) 18422–18436, <https://doi.org/10.1021/jacs.0c06668>.
- [81] S.P. Ong et al., *Energy Environ. Sci.* 6 (1) (2012) 148–156, <https://doi.org/10.1039/c2ee23355j>.
- [82] B. Chen et al., *Comput. Mater. Sci.* 153 (2018) 170–175, <https://doi.org/10.1016/j.commatsci.2018.06.041>.
- [83] Y. Qi, C. Ban, S.J. Harris, *Joule* 4 (12) (2020) 2599–2608, <https://doi.org/10.1016/j.joule.2020.10.009>.
- [84] C. Ren et al., *Sci. China Mater.* 64 (9) (2021) 2348–2358, <https://doi.org/10.1007/s40843-021-1648-3>.
- [85] W.H. Kan et al., *Chem* 4 (9) (2018) 2108–2123, <https://doi.org/10.1016/j.chempr.2018.05.008>.
- [86] A. King et al., *Science* 321 (5887) (2008) 382–385, <https://doi.org/10.1126/science.1156211>.
- [87] H. Simons et al., *Nat. Commun.* 6 (2015) 6098, <https://doi.org/10.1038/ncomms7098>.
- [88] J. Zhang et al., *Acta Mater.* 191 (2020) 211–220, <https://doi.org/10.1016/j.actamat.2020.03.044>.
- [89] H. Simons et al., *Nat. Mater.* 17 (9) (2018) 814–819, <https://doi.org/10.1038/s41563-018-0116-3>.
- [90] D.P. Finegan et al., *Nat. Commun.* 11 (1) (2020) 631, <https://doi.org/10.1038/s41467-020-14467-x>.
- [91] D.P. Finegan et al., *Nano Lett.* 19 (6) (2019) 3811–3820, <https://doi.org/10.1021/acs.nanolett.9b00955>.
- [92] H. Dong et al., *NPJ Comput. Mater.* 7 (2021) 74, <https://doi.org/10.5281/zenodo.4664597>.
- [93] A. Vamvakeros et al., *J. Appl. Crystallogr.* 49 (2016) 485–496, <https://doi.org/10.1107/S160057671600131X>.
- [94] J. Sharf et al., *Nat. Nanotechnol.* (2022), <https://doi.org/10.1038/s41565-022-01081-9>.
- [95] A. Vamvakeros et al., *Nat. Commun.* 9 (1) (2018) 1–11, <https://doi.org/10.1038/s41467-018-07046-8>.
- [96] G.A. Buzanich, *X-Ray Spectrom.* 51 (2022) 294–303, <https://doi.org/10.1002/xrs.325>.
- [97] S. Spence et al., *Nanotechnology* 32 (2021), <https://doi.org/10.1088/1361-6528/ac17ff.442003>.
- [98] I. Álvarez-Clemares et al., *Scripta Mater.* 68 (8) (2013) 603–606, <https://doi.org/10.1016/j.scriptamat.2012.12.016>.
- [99] J. Guo et al., *Adv. Funct. Mater.* 26 (2016) 7115–7121, <https://doi.org/10.1002/adfm.201602489>.
- [100] J. Guo et al., *Adv. Mater.* 30 (2018) 1801846, <https://doi.org/10.1002/adma.201801846>.
- [101] C.-S. Jiang et al., *Adv. Energy Mater.* 10 (2020) 2000219, <https://doi.org/10.1002/aenm.202000219>.
- [102] L. Baggetto et al., *Adv. Funct. Mater.* 18 (7) (2008) 1057–1066, <https://doi.org/10.1002/adfm.200701245>.
- [103] K.J. Kim, J.L.M. Rupp, *Energy Environ. Sci.* 13 (12) (2020) 4930–4945, <https://doi.org/10.1039/d0ee02062a>.
- [104] K. Fu et al., *Energy Environ. Sci.* 10 (7) (2017) 1568–1575, <https://doi.org/10.1039/c7ee01004d>.
- [105] D.W. McOwen et al., *Adv. Mater.* 30 (18) (2018) e1707132, <https://doi.org/10.1002/adma.201707132>.
- [106] H. Shen et al., *J. Mater. Chem. A* 7 (36) (2019) 20861–20870, <https://doi.org/10.1039/C9TA06520B>.
- [107] H. Shen et al., *ACS Appl. Mater. Interfaces* 12 (3) (2020) 3494–3501, <https://doi.org/10.1021/acsami.9b11780>.
- [108] E. Yi et al., *ACS Appl. Energy Mater.* 3 (1) (2020) 170–175, <https://doi.org/10.1021/acsami.9b02101>.
- [109] J. Zhu et al., *Angew. Chem. Int. Ed. Engl.* 60 (7) (2021) 3781–3790, <https://doi.org/10.1002/anie.202014265>.
- [110] R. Pfenninger et al., *Nat. Energy* 4 (6) (2019) 475–483, <https://doi.org/10.1038/s41560-019-0384-4>.